Unveiling field-coupled nanocomputing: Leaning molecules to shape readable bits

Nano Research
2024, 17(9): 8447–8454

ISSN 1998-0124 CN 11-5974/O4
https://doi.org/10.1007/s12274-024-6811-2

Research Article

Unveiling field-coupled nanocomputing: Leaning molecules to shape readable bits

Yuri Ardesi[1] (✉), Giuliana Beretta[1], Fabrizio Mo[1], Chiara Elfi Spano[1], Gianluca Piccinini[1], and Mariagrazia Graziano[2]

[1] *Corso Duca degli Abruzzi, Department of Electronics and Telecommunications, Politecnico di Torino, Turin 10129, Italy*
[2] *Corso Duca degli Abruzzi, Department of Applied Science and Technology, Politecnico di Torino, Turin 10129, Italy*

Received: 5 April 2024 / **Revised:** 24 May 2024 / **Accepted:** 4 June 2024

ABSTRACT

Molecular field-coupled nanocomputing (molFCN) encodes information in the molecule charge distribution and elaborates it through electrostatic coupling. Despite the advantageous sub-nanometric size and low-power dissipation, only a few attempts have been made to validate the technology experimentally. One of the obstacles is the difficulty in measuring molecule charges to validate information encoding or integrate molFCN with complementary-metal-oxide-semiconductor (CMOS). In this work, we propose a paradigm preserving the advantages of molFCN, which exploits the position of waiving molecules to augment the information encoding. We validate the paradigm, named bend-boosted molFCN, with density functional theory using 6-(ferrocenyl)hexanethiol cations. We demonstrate that the encoded information can be electrically read by constituting a molecular junction. The paradigm is compatible with the charge-based molFCN, thus acting as a readout system. The obtained results favor the experimental assessment of the molFCN principle through scanning probe microscopy techniques and the design of molFCN-CMOS heterogeneous circuits.

KEYWORDS

nanoelectronics, molecular electronics, field-coupled nanocomputing, electronics, beyond-complementary-metal-oxide-semiconductor (CMOS)

1 Introduction

The approaching complementary-metal-oxide-semiconductor (CMOS) scaling limits push scientists to investigate novel digital nanocomputing technologies based on brand-new working principles governed by quantum physics. The quantum-dot cellular automata (QCA) paradigm exploits cells of four quantum dots arranged in a square [1, 2], populated by electrons located on the antipodal dots thanks to Coulomb's force, thus in two possible states encoding logic "0" and "1", as Fig. 1(a) shows.

The QCA paradigm can be implemented using molecules, constituting the molecular field-coupled nanocomputing (molFCN) paradigm. The information is encoded in the molecular charge distribution and propagates through intermolecular electrostatic interactions [3, 4]. For clarity, we refer to this paradigm as charge-based molFCN to distinguish it from the bend-boosted molFCN proposed in this work, which encodes the information in molecule charge and bending.

Using bis-ferrocene as an example [5], Fig. 1(a) shows the charge-based molFCN cell composed of two cations [6]. The intermolecular electrostatic repulsion forces the electron clouds, shown in Fig. 1(a) with colored blobs, in two energy-equivalent configurations mimicking the QCA paradigm. In addition, a possible electric field named clocking field pushes the charge distribution to the molecule bottom, erasing information and creating the so-called "NULL" state [4]. The electrostatic interaction among nearby cells enables information propagation and elaboration through specific patterns. Figure 1(b) shows a wire of eight cells, where the clocking field drives the information propagation. Figure 1(c) shows a majority voter: a fundamental device implementing the majority function that can be used to realize OR and AND operations. Figure 1(d) shows the NOT gate. Combining basic gates permits the design of more complex logic circuits [7].

Numerous simulations and theoretical analyses demonstrate promising advantages in molFCN. The nanometric extension leads to highly dense device designs [2]. Then, the absence of current grants very low power consumption, remaining mainly imputable to the clocking mechanism [8, 9]. Finally, molFCN can hold high-frequency switching [10, 11] and work at ambient temperature [11, 12]

Despite the advantages, the realization of a working prototype is mainly obstructed by the complex syntheses of ad-hoc molecules, the precise nanopatterning of molecules and electrodes, and the reading of the charge-encoded informations [5, 13, 14]. In a recent study, we proposed to perform computation directly on self-assembled monolayers to overcome the need for molecular nanopatterning [15]. Besides, few works experimentally measured the molecule charge through advanced scanning probe microscopy (SPM) techniques, promising for in-lab assessment of molFCN [16, 17]. Finally, a recent study proposed a system based on asymmetric mixed-valence molecules for in-circuit reading [18]. Nevertheless, no definitive solution permits the electrical detection of the charge-encoded information.

This work presents a molFCN implementation that simplifies the in-circuit and in-lab molFCN readout operations. Indeed, the

Address correspondence to yuri.ardesi@polito.it

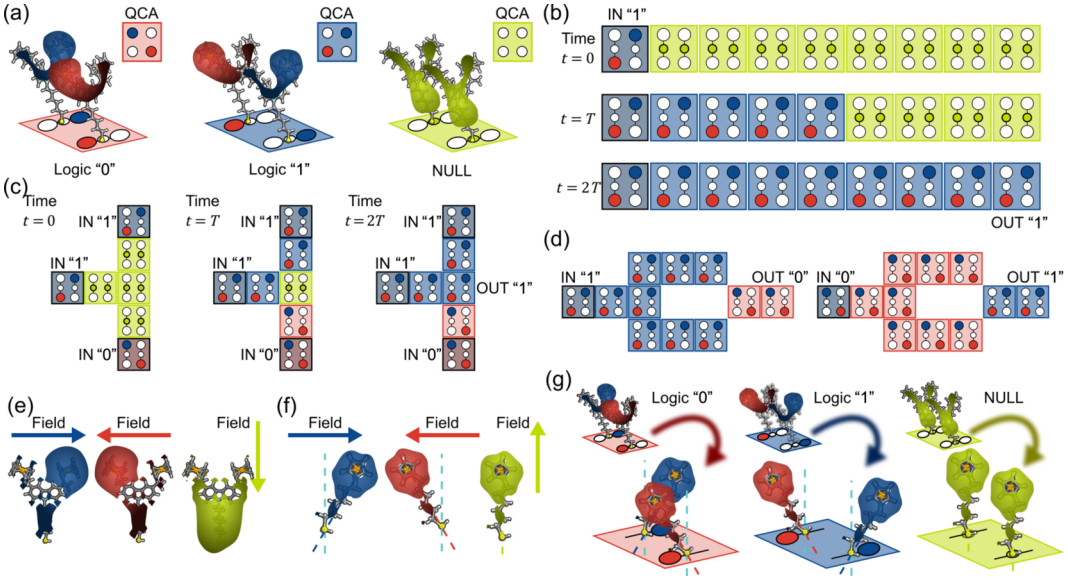

Figure 1 Fundamentals of the molFCN and proposed paradigm. (a) Molecular cells made with two bis-ferrocene cations encoding the three possible logic states "0", "1", and "NULL", respectively, according to the here named charge-based molFCN technology. (b) Propagation through a molFCN wire, sampled at subsequent time steps to show information guided by the clocking field. (c) Propagation in a clocked molFCN majority voter implementing the majority voting operation on inputs "1", "1", and "0", with output "1". (d) MolFCN inverter performing the NOT operation on binary logic "0" and "1". (e) Charge distribution of the bis-ferrocene molecule in the classical charge-based molFCN paradigm and relative electric field creating the charge displacement. (f) Bending of the FcC_6S molecule in the proposed bend-boosted molFCN paradigm and related electric field creating the molecule bending. (g) Equivalence of the unit cells encoding the logic values for the two paradigms.

charge-based molFCN paradigm exploits fixed molecules that encode the logic information only in their charge distribution dictated by an impinging electric field, as Fig. 1(e) shows. We propose a paradigm that exploits the molecule bending to encode the information, following the concept introduced in [19] and naming it bend-boosted molFCN paradigm. We use the 6-(ferrocenyl)hexanethiol cation as a reference molecule, hereafter denoted FcC_6S. Figure 1(f) schematically shows the application of an electric field to the anchored FcC_6S, which provokes the cation bending associated with logic information, enabling the write-in operation. Later, we demonstrate that the ferrocene loses the electron for oxidation, leaving a positive charge aggregation on it, as Fig. 1(f) shows. Figure 1(g) shows that the electrostatic repulsion forces two juxtaposed FcC_6Ss to bend in opposite directions, giving two distinct configurations for a cell to encode logic information equivalent to charge-based molFCN.

The association of information with different molecule orientations eases the in-lab read-out, potentially performed through established atomic-precise topographic measurements [20–22]. This work demonstrates the encoding capabilities of the proposed paradigm using density functional theory (DFT) and molecular dynamics (MD). Then, we analyze the conductive properties of a FcC_6S molecular junction, used as a single-molecule sensor. Indeed, single-molecule junctions have been theoretically demonstrated as sensors of nanometric electro-static interactions [23, 24]. We demonstrate with non-equilibrium Green's functions (NEGF) formalism the current modulation in a molecular junction according to the information encoded, thus providing in-circuit readout capabilities that permit the assessment of molFCN technology and its integration with CMOS.

2 Results and discussion

2.1 Binary encoding in 6-(ferrocenyl)hexanethiol

The chemical structure of the FcC_6S cation used in this work is reported in Fig. 2(a). Figure 2(b) reports a three-dimensional (3D) scheme of the molecule and its functional division in two sub-parts: the ferrocene (Fc) and the hexanethiol (C_6S). First, we simulated the FcC_6S with DFT precision to obtain the reference geometry, shown in Fig. 2(c) (see Table S1 in the Electronic Supplementary Material (ESM) for the atom coordinates).

Secondly, since molFCN exploits electrostatic capabilities to elaborate information, we analyze the electrostatic properties of the molecules. The molecular electrostatic potential evaluated with DFT and depicted in Fig. 2(d), presents a maximum value on the ferrocene, denoting a positive charge aggregation. The sum of the atomic charges of the two functional groups, defined in Fig. 2(b), yields the aggregated charge (AC) [25]. The AC value on the ferrocene equals Q_{Fc} = 0.9595 a.u., confirming a positive charge aggregation in the ferrocene, whereas the hexanethiol results neutral (Q_{C6S} = 0.0405 a.u.), meaning that the ferrocene dictates the motion of the cation in an electric field. Suppose the molecule is anchored to a gold substrate through the thiol (–SH) as reported in Refs. [26, 27]. In that case, the hexane acts as a rigid bar linking the ferrocene to the substrate, constraining the possible molecule motion to a rotation around the thiol.

Following the typical approach of FCN studies [3, 28], this work does not consider the substrate since we are interested in studying the encoding paradigm solely dictated by the molecule, thus isolating the working principle from possible external stimuli. We expect the substrate to influence the molecule behavior, yet we postpone this analysis to future works and concentrate on the working principle. To validate the logic encoding, the FcC_6S cation is studied with *Ab initio* molecular dynamics (AIMD) to analyze it immersed in electric fields in the time domain. The applied fields are constant values equal to ±4.9451 V/nm (see Sec. S2 of the ESM for details). The field value is chosen to limit the computational time required by the DFT calculation to simulate the complete bending of the molecule. Later in this section, classical molecular dynamics simulations will validate the paradigm on lower electric fields and more extended time.

Figure 2(e) shows the effect calculated with AIMD of the constant electric field E_y = 4.9451 V/nm oriented along the positive *y*-axis. In particular, the blue dots represent the initial conformation of the cation, positioned perpendicular to a fictitious ideal substrate (i.e., in a NULL configuration) with the thiol –SH fixed to it. In contrast, the red points show the molecule after 3 ps,

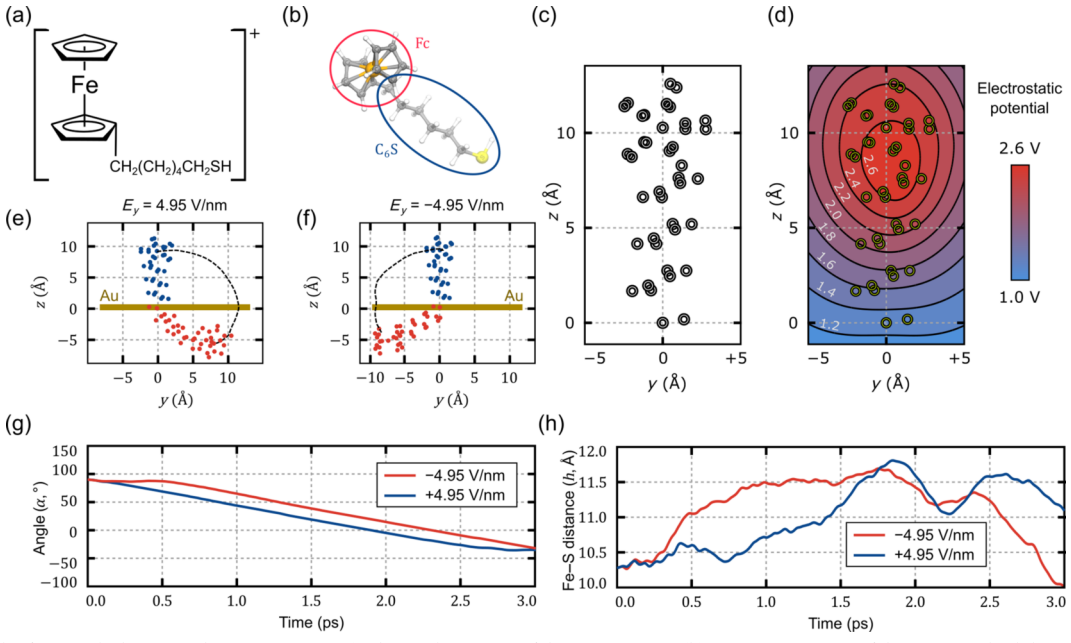

Figure 2 Result of DFT calculation on the FcC_6S cation. (a) Chemical structure of the FcC_6S cation. (b) 3D representation of the FcC_6S and subdivision in functional groups. (c) Cartesian coordinates of the FcC_6S cation obtained with DFT relaxation. (d) Molecular electrostatic potential evaluated for the FcC_6S cation with DFT calculation, the solid black lines are isopotential curves. (e) AIMD analysis of the FcC_6S cation when subjected to a positive electric field (E_y = 4.95 V/nm). The black dotted line represents the movement of the Fe atom from the starting position (blue dots) and after 3 ps (red dots). The molecule rotates clockwise around the thiol group SH, fixed on the fictitious substrate Au line. (f) AIMD analysis of the FcC_6S cation when subjected to a negative electric field (E_y = −4.95 V/nm). The black dotted line represents the movement of the Fe atom from the starting position (blue dots) and after 3 ps (red dots). The molecule performs a counterclockwise rotation around the thiol group –SH, fixed on the fictitious substrate Au line. (g) Evolution in time of the molecule angle (α) evaluated between the Fe–S segment and the fictitious substrate Au line during the AIMD calculation. (h) Evolution in time of the Fe–S distance during the AIMD calculation.

confirming that the molecule bends according to the field direction by rotating clockwise around the anchored thiol –SH. Since the substrate is missing in the AIMD simulations, no substrate-molecule interaction exists, and the molecule overcomes the ideal substrate line indicated in yellow in Fig. 2(e). Similarly, Fig. 2(f) shows the effect of an opposite field (−4.9451 V/nm) parallel to the y-axis. The molecule performs a comparable movement in the opposite direction, demonstrating the encoding capability.

Figure 2(g) reports the angle (α) between the S–Fe segment and the Au line (z = 0) evaluated during the simulation. Aiming to have comparable values, we refer the angle measurements to the positive y-axis for the clockwise rotation and the negative y-axis for the counterclockwise rotation. The maximum angle (α = 90°) represents the molecule in the NULL state. Figure 2(g) demonstrates that clockwise and counterclockwise rotations differ in terms of behavior in the first 0.5 ps of the dynamics. The first time period, here referred to as warm up time, can be considered a non-ideal behavior of the molecule, which has to rearrange the atoms to start the molecule bending. After the warm up, the molecule demonstrates a linear bending dynamic (ideal regime), whose speed is 0.0528°/fs for the negative field value, and 0.0522°/fs for the positive one. The warm-up time is larger for the negative electric field. We believe this is due to a slight bending of the hexanethiol towards positive y values at the equilibrium. Therefore, when the negative electric field is applied, the hexanethiol firstly has to align with the z-axis, making the warm-up time longer. On the contrary, the initial bending favors the clockwise rotation, reducing the warm-up time.

For the paradigm definition, the boundaries of the encoding dynamic range correspond to angles α = 90° and α = 0°. So, the encoding time (τ_e) is evaluated as the time required to move from α = 81° to α = 9° (i.e., 90% and 10% of the total encoding dynamic, respectively) in the ideal regime. We obtain an encoding time $\tau_{e,cw}$ = 1381.4180 fs for the positive field (clockwise rotation), and $\tau_{e,ccw}$ = 1421.6907 fs for the negative field (counterclockwise rotation). On average, molecule switches in $\bar{\tau}_e$ = 1401.5544 fs.

To estimate the maximum switching frequency, we imagine driving the molecule from the NULL state (α = 90°) to encode a particular logic value and then deleting it to reproduce an entire switching operation. For example, we consider the molecule leaning to α = 0° (clockwise rotation) and then standing up toward the NULL state configuration with a counterclockwise rotation. Similarly to the encoding time, the reset time (τ_r) is the time required to move the molecule from 9° to 81°. The simulations described above show that the clockwise and counterclockwise rotations are not perfectly equivalent since we constrained both the S atom and its H. Thus, for consistency, we should simulate the molecule starting with α = 0° with an electric field perpendicular to the substrate line to evaluate τ_r. Although the switching times differ for the two rotations, the order of magnitude is the same, so we approximate the reset time to the switching time corresponding to the same rotation. In other words, if the encoding time is $\tau_{e,cw}$, the reset time is approximately equal to $\tau_{e,ccw}$ and vice versa. Therefore, the complete switching operation is performed in a time equal to $\tau_{e,cw} + \tau_{e,ccw}$, giving a switching frequency (f_{sw}) for E_y = ±4.9451 V/nm of

$$f_{sw} \approx \frac{1}{\tau_{e,cw} + \tau_{e,ccw}} = 356.747 \text{ GHz} \quad (1)$$

The value obtained gives a first-order estimation of the obtainable switching frequency. Along with approximating the reset time as the encoding time with the same rotation, the simulations are performed without a substrate that may attract/repulse the molecule, thus accelerating/slowing down the effective dynamics. Moreover, the encoding time does not consider possible delays in the first and last femtoseconds, such as the time the molecule needs to move out of the equilibrium. Conversely, it is possible to achieve encoding with lower angles, permitting a reduction of the switching time.

As a final consideration, Fig. 2(h) reports the Fe–S distance (h). The average strains for the two fields are 1.1131 and 1.1026 Å, whereas the equilibrium value is h = 1.0283 nm, i.e., the relative strain is 10.8% and 10.7%, respectively. The obtained results

demonstrate that the molecule is mostly non-strained during the movement, denoting a rigid-bar behavior of the hexanethiol.

The obtained result demonstrates that it is possible to use electric fields to encode information in the FcC_6S bending, and lowering the electric field would reduce the power dissipation associated with it. We study the system subjected to lower fields with MD to reduce the computational cost, starting with the field values used in the AIMD simulations to validate the procedure. So, using the same initial configuration, we simulate the dynamics for 3 ps applying $E_y = 4.9451$ V/nm and $E_y = -4.9451$ V/nm. Since AIMD simulations prove the molecule to be approximately rigid during the bending, the molecule is considered a rigid system except for S in MD simulations. The only permitted movements are stretches of the S-molecule bond and rotations around the sulfur joint, imagining it linked to a substrate.

Figure 3(a) shows the superposition of the molecule final configurations obtained with AIMD and MD after 3 ps, and the path followed by the iron atom. The last configurations are similar in both the comparisons, and the main differences are relatable with the molecule rigidity in MD. Indeed, the iron path differs the most when the molecule aligns to the *y*-axis. In this position, the molecule is subjected the most to the applied electric field, causing some deformations in the molecule. In the MD simulations, this defor- mation can only be translated into an elongation of the bond between S and the hexane since the rest of the system is rigid. Besides the highly simplified model used for MD, the trajectory follows the more precise AIMD calculation.

Figure 3(b) continues the comparison by showing the angle between the molecule and the $z = 0$ plane during both AIMD and MD simulations, highlighting the points where $\alpha = 0°$. The MD curves are almost identical for both the positive and negative fields due to the rigid system. Also, the curve steepness is comparable in AIMD and MD for both fields. For the two MD simulations, the encoding times are $\tau_{e,cw} = 1495.4204$ fs for the positive field (clockwise rotation) and $\tau_{e,ccw} = 1488.5061$ fs for the negative field (counterclockwise rotation), giving a lower switching frequency than AIMD ($f_{sw} \approx 335.129$ GHz evaluated with Eq. (1)). The main difference between AIMD and MD is found in the warm up time, impacting the switching time values. Indeed, in AIMD simulations, the initial resistance of the molecule to the movement depends on the direction of the applied field. In contrast, the initial resistance is lost in MD for the model simplification. The variation on the first instants leads to differences in the angle. Figure 3(c) shows the differences of the angle between AIMD and MD simulations for both positive and negative electric fields. The error may be substantial (~ 15°) during the transient, mainly due to the rigid molecule model assumption. Nevertheless, the trajectory followed by AIMD and MD is the same, and the error is recovered toward the end of the simulation, confirming the possibility of using MD to estimate the behavior of the paradigm with small losses in precision.

Since AIMD and MD results are consistent, but MD simulations are faster, we use them to validate the behavior for various applied electric field, evaluating the switching time.

Figure 3(d) shows the angles the molecule creates with the plane $z = 0$. Reducing the field intensity slows down the molecule bending. In addition, due to the different warm up times for negative and positive electric fields, reducing the field accentuates differences between opposite signs of the same field. As already mentioned, the warm up time is indeed longer for negative electric field, impinging on the encoding dynamics. The lower, in absolute terms, the negative electric field, the higher the warm up time and the overall switching time. It is important to notice that, notwithstanding the slightly different behavior for low electric field, the principle of the paradigm is preserved. For smaller fields, the angle needs more time to cross the $z = 0$ plane where we place

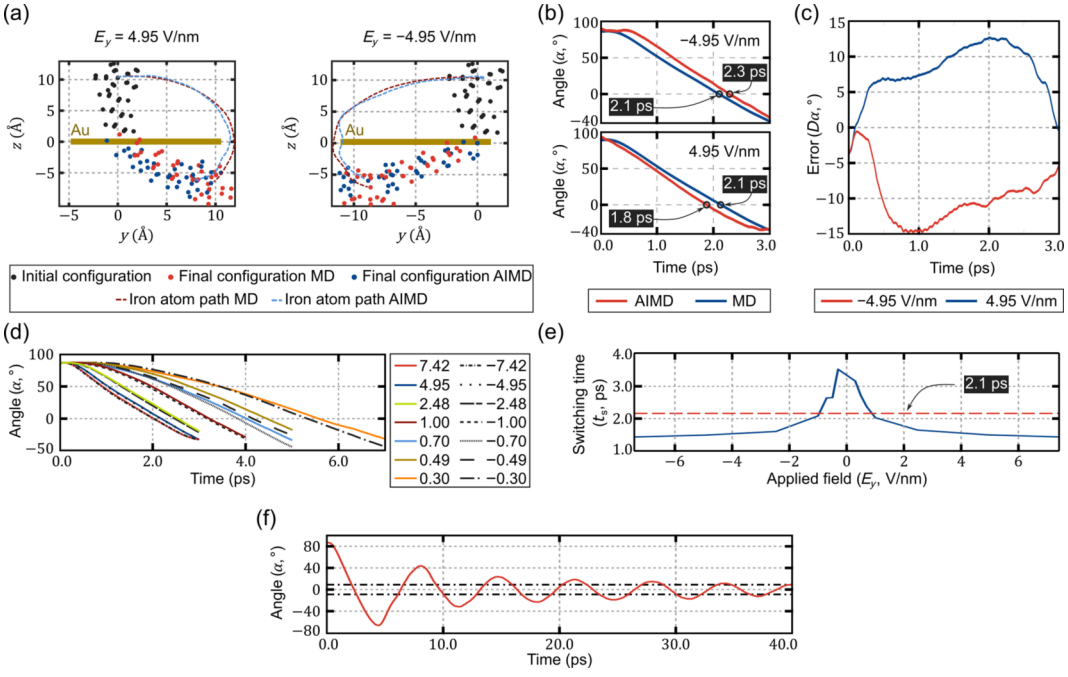

Figure 3 Result of MD calculation on the FcC_6S cation. (a) Comparison of AIMD and MD trajectories of the FcC_6S cation when subjected to positive and negative electric fields. The light blue/dark red dotted line represents the movement of the Fe atom in the AIMD/MD simulation from the starting position (black points) and after 3 ps (blue/red points). (b) Comparison of the angle created by the FcC_6 cation in time for AIMD and MD simulations, with both a positive and a negative electric field. The points highlighted identify the time value where the angle α equals 0°. (c) Absolute error between MD and AIMD in the angle of the FcC_6S with the substrate for both positive and negative driving electric fields. (d) Angle of the FcC_6 with the substrate calculated with MD for different electric fields. The smaller the applied field, the slower the molecule reaches the substrate. (e) Switching time evaluated as the difference between the time needed to move from an angle of 81° to 9° (i.e., 90% and 10% of the total dynamic, respectively) varying the intensity of the electric field. (f) Angle of the FcC_6S with the substrate calculated with a long MD simulation when the driving field equals 2.48 V/nm. The angle oscillated around 0°, which is the expected regime value. The black dotted line identifies the range between −9° and 9° (i.e., ±10% of the switching dynamic).

the hypothetical substrate. Figure 3(e) shows the switching time varying the driving electric field. The dashed line identifies the average encoding time $\tau_{e,\mu}$ = 2.1 ps. The curve confirms that reducing the applied field intensity increases the switching time. For example, by applying a field E_y = −0.4945 V/nm, we find $f_{sw} \approx$ 186.440 GHz using Eq. (1), so reducing the applied field by ten just halves the frequency. Besides, the switching time settles to a constant value when increasing the electric field. Over a certain threshold, increasing the driving field leads to power consumption growing without obtaining better frequency performance. For example, with E_y = −7.4177 V/nm, we get $f_{sw} \approx$ 349.075 GHz, meaning that by increasing the field by 33%, the frequency rises roughly 4%.

Finally, we exploit MD simulations to verify how the molecule behaves in a time longer than those used so far. By applying an electric field along the *y*-axis, we expect the FcC_6S to align with the substrate line. Figure 3(f) shows the damping angle oscillations around the y-axis when the driving electric field equals 2.48 V/nm. The dashed lines identify the region where oscillations settle below 9°, i.e., 10% of the encoding dynamic. This simulation confirms that the molecule aligns with the applied field. Moreover, the angle reaches the regime value as an underdamped second-order system (two complex conjugate roots). By including a substrate, we expect it to influence the molecule behavior. In particular, attraction and repulsion of the substrate may accelerate or slow down the bending of the molecule and change the settle angle. Future work should address the electrostatic influence of the substrate and the possible charge exchange between the two actors. Different materials should also be addressed.

2.2 The bend-boosted paradigm as a charge sensor

All the analyses shown in section demonstrate that an electric field can write binary information into the molecule bending. Possible cations can generate an electric field potentially driving adjacent molecules, thus enabling information propagation, given that the steric hindrance during the rearrangement is overtaken. A detailed analysis of logic propagation and elaboration is postponed to following studies. Regarding the readout capabilities, the bend-boosted molFCN mechanism enables the detection of the encoded information at the laboratory level by measuring the molecule orientation through SPM [22].

The bend-boosted molFCN can also be integrated with the charge-based paradigm. Indeed, previous studies reported that the bis-ferrocene cation generates [−0.4, 0.4] V/nm switching fields [25], which are sufficient to drive the bending mechanism, as demonstrated in Sec. 2.1. Therefore, the electric field generated by the bis-ferrocene cation, taken as an example, may act as a driving signal for the FcC_6S. Bend-boosted molFCN interfaced with the charge-based, permits in-lab measurement of charge-based molFCN logic with SPM, favoring the assessment of charge-based molFCN technology.

This section demonstrates that bend-boosted molFCN also favors the integration of molFCN with CMOS technology. Figure 4(a) shows the system for the information readout, where a single cation anchored on a nanowire (NW) in a metallic nanogap is adjacent to a charge-based molFCN circuit. The metallic nanogap electrodes, here denoted as E0 and E1 electrodes, permit a tunneling current between the E1 (or E0) and the NW through

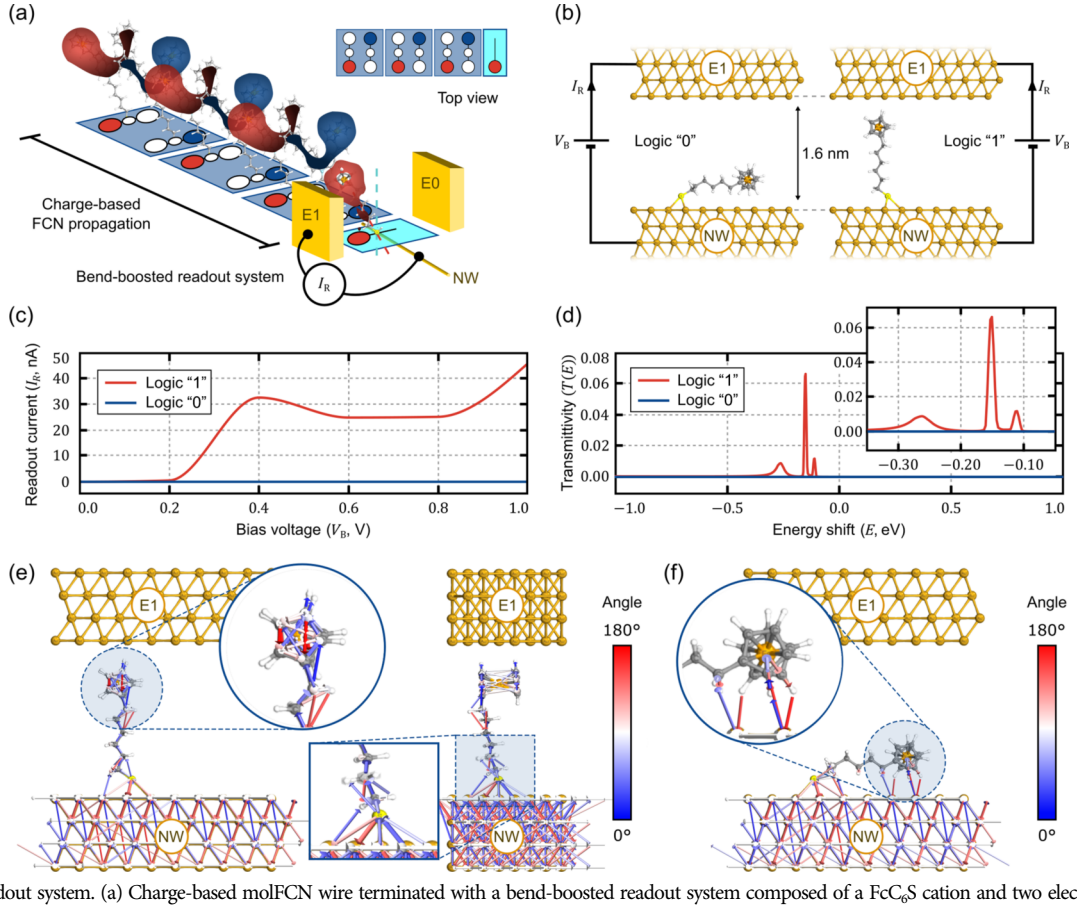

Figure 4 Readout system. (a) Charge-based molFCN wire terminated with a bend-boosted readout system composed of a FcC_6S cation and two electrodes (E0, E1) for the conductive measurement. Molecules are supposed anchored to an ideal NW. The schematic amperometer measures the I_R. (b) Geometries used to study the conduction between the electrode E1 and the NW with DFT precision. In the left figure, the cation encodes a logic "0" (far from the E1 electrode), whereas in the right figure the cation encodes a logic "1" (close to the E1 electrode). A V_B is applied between E1 and NW. (c) I_R calculated with DFT between E1 and NW when the FcC_6S encodes the two logic values. (d) Transmission spectrum (T) calculated with DFT when the FcC_6S encodes the two logic values. The inset shows an enlargement of the transmittivity where is non-zero. (e) Transmission pathways for the electrons transmitted from the NW to E1 electrode when the cation encodes a logic "1". (f) Transmission pathways for the electrons transmitted from the NW to E1 electrode when the cation encodes a logic "0".

the molecule. The encoded information varies the orientation of the FcC_6S, thus its distance from the electrodes. When the molecule encodes logic "1", the ferrocene will approach E1, enhancing the tunneling current through the E1 electrode and drastically reducing the one through E0. Vice versa, logic "0" brings the Fc close to E0. This working principle is modeled by a FcC_6S single-molecule junction, with the two configurations shown in Fig. 4(b). The two conformations result from a geometrical relaxation of the already optimized FcC_6S, and correspond to logic "0" (Fc away from E1) and logic "1" (Fc close to E1), respectively. The cation is anchored onto a face-centered-cubic (111) gold substrate (10 × 4 atoms slab). The E1-to-NW distance is 1.6 nm, and E1 and NW contacts are made with gold.

To validate the readout structure, we evaluate the electronic transport of the junction with DFT and NEGF. Figure 4(c) reports the obtained readout current (I_R) evaluated as a function of the bias voltage (V_B) applied between E1 and NW for both the configurations. The logic "1" configuration presents a significant current I_R. For instance, working with V_B = 0.4 V provides I_R = 32.53 nA. On the contrary, the logic "0" configuration provides zero current, permitting distinguishing the logic states. By investigating the transmission spectrum $T(E)$, we examine the origin of the current difference. Figure 4(d) reports T as a function of the energy shift (E) at fixed V_B = 0.4 V. E = 0 eV is the system equilibrium Fermi level. The inset in Fig. 4(d) focuses on $T(E)$ in the range [−0.4, 0] eV. A finite electron transmission probability occurs in the logic "1" configuration, with a $T(E)$ = 0.682 at E = −0.15 eV. Transmittivity peaks are located at negative energies, i.e. occupied FcC_6S molecular orbitals. The conduction is dominated by the highest occupied molecular orbital (HOMO). On the other hand, the logic "0" configuration has a null electron transmission probability at every considered energy value, leading to the null I_R.

The negative differential resistance (NDR) in the range [0.4, 0.6] V and the I_R plateau in the range 0.6–0.8 V, for the logic "1" configuration, are both caused by the significant charging of the FcC_6S induced by the applied V_B. Figure S2 in the ESM reports the full $T(E,V_B)$ contour plot. For increasing V_B the relevant transmission peaks undergo to an energy shift highlighted by the arrow, constituting the signature of the charging effect. In addition, the charging modifies the magnitude of the transmission function that in the range [0.4, 0.6] V decreases, originating the NDR, and then is stable in [0.6, 0.8] V, causing the I_R plateau (dashed circle). From V_B = 0.8 V on, the $T(E,V_B)$ peaks increase again, and I_R increases again.

By analyzing the NW-to-E1 transmission pathways (TP) at V_B = 0.4 V and E = −0.15 eV, we identify the origin of the $T(E)$ differences between the logic "0" and logic "1" cases. The TPs [29] provide information on local contributions to $T(E)$. Both the propagating direction (arrow direction) and the transmission probability (arrow size) are represented. Figure 4(e) reports the TPs for the logic "1" configuration, front and lateral views (enlargements are provided in Figs. S3 and S4 in the ESM). Transmission is very probable from NW to the sulfur atom (large arrows) and less probable through the saturated chain (small arrows). For the visualized transmission probability value, no arrows are linking the ferrocene to E1 (tunneling barrier). Arrows are visible when much lower transmission probability is displayed, indeed a finite $T(E)$ is present. The obtained result matches the expectations: the anchoring sulfur atom contributes with well-delocalized states, thanks to its covalent bond with gold. The saturated hexanethiol presents localized orbitals with small transmission probability along the carbon atoms (sigma orbitals). Good delocalization is present in the ferrocene (many and relatively large arrows) thanks to Fe and cyclopentadiene π-type orbitals. The transmission bottleneck is the tunneling barrier between FcC_6S and E1. The FcC_6S molecule behaves as a molecular bridge between NW and E1 in the logic "1" configuration, with only a small tunneling barrier.

On the contrary, with logic "0", Fig. 4(f), the FcC_6S does not act as a molecular bridge. Despite the significant electron transmission between NW and sulfur, the molecule rotation leads to negligible transmission along the hexane chain. Few and small TP arrows, directed toward the NW, connect NW and Fc. Therefore, electrons at NW should overcome a tunneling barrier of the order of the NW-E1 distance, making $T(E)$ negligible.

The substrate can act as a parallel resistance to the molecular junction. We expect a detectable current difference in the two logic configurations of the order of 30 nA (for $V_B \geq 0.4$ V). The clear I_R separation in the two logic states demonstrates the successful readout system. The readout reliability can be affected by additional external factors. For example, an external electric field generated by nearby electrodes can affect the molecule positioning. Future works should account for the external factors on the readout capabilities to verify the robustness of the revealing mechanism.

The results obtained in this work demonstrate the advancement on readout systems made by the bend-boosted molFCN paradigm, contributing to the possible integration of molFCN with CMOS by exploiting single-molecule junctions.

3 Conclusion

We reported a new computational paradigm named bend-boosted molFCN, which enhances the charge-based molFCN by encoding the information in molecule bending and charge distribution. We demonstrated the information encoding in the bending of a FcC_6S cation with a theoretical switching frequency that reaches 357 GHz and can be adjusted by setting the applied field to optimize the speed-dissipation trade-off. The bend-boosted molFCN is compatible with charge-based FCN technologies, paving the way for the validation of molFCN. Indeed, including the bending angle in the encoding facilitates the experimental validation of the molFCN technology by providing measurability through scanning probe microscopy. The proposed paradigm may work as a readout system for charge-based molFCN. Indeed, FcC_6S singlemolecule junctions show different currents according to the encoded logic, thus providing possible future integration with CMOS by interfacing charge-based molFCN molecules with the molecular junction, used as charge sensors. The current work addressed the peculiar characteristics of the bend-boosted paradigm by analyzing the isolated cation. Future work should address the substrate effect, the role of molecule hindrance, and the electrostatic interaction in the possible propagation of the information. This work sets a milestone for the molFCN. Indeed, the results favor the realization of a prototype by providing a means for technology validation, assessment, and integration.

4 Methodology

4.1 Molecular modeling

The theoretical modeling of the molecules is based on the MoSQuiTo methodology, which permits studying molecules from an electronics perspective [25]. The methodology consists of three steps: physical characterization, derivation of the figure of merits, and the possible circuit analysis, generally performed with the SCERPA tool [30, 31].

4.2 *Ab initio* characterization

Ab initio geometry optimization and single-point calculation are performed using the ORCA Package [32, 33]. Calculations on the

isolated FcC_6S cation are done with the unrestricted KohnShann (UKS) method using Becke3 Lee–Yang–Parr (B3LYP) functional with def2-TZVP basis set [34]. Grimme D3 correction is applied [35, 36].

4.3 Electrostatic analysis

The FcC_6S cation charge distribution is analyzed by exploiting the CHELPG paradigm. The ORCA tool calculates the electrostatic potential generated by the molecule, and a set of atom-centered charges is obtained by fitting the electrostatic potential [37]. Therefore, atomic charges are summed up in groups to obtain the so-called AC distribution [25]. The value of AC is normalized to the electron charge ($q = 1.60 \times 10^{-19}$ C).

4.4 *Ab initio* dynamic field effect analysis

The evolution of the FcC_6S cation geometry in the time domain is analyzed with AIMD. The thiol SH is fixed in the space to emulate the anchoring of the molecule to the substrate. No constraints are applied to the remaining atoms, which are free to move. External electric fields are applied in the simulation to emulate the action of external electrodes or other molecules. The ORCA tool does not permit the introduction of a uniform electric field. Therefore, following the method adopted in previous studies [9, 12], the electric field is emulated through point charges (see Sec. 2 in the ESM for details). AIMD calculation is performed with the UKS method and B3LYP/SVP level of theory. Grimme D3 correction is not applied. AIMD calculation has been speed-up with RIJCOSX, employing auxiliary basis set def2/J [38].

4.5 Molecular dynamics analysis

Molecular dynamics calculations are performed using the large-scale atomic/molecular massively parallel simulator (LAMMPS) software package [39]. Calculations are performed using the ReaxFF potential of van Duin, Goddard, and co-workers [40]. Calculations follow NVT dynamics using the velocity-Verlet time integration algorithm and the Nosé-Hoover thermostat. The ferrocene and the hexane are considered rigid during the simulations, whereas the sulfur atom is fixed in the initial position emulating the anchoring to a substrate.

4.6 Electronic transport characterisation

The configurations used for the transport measurement are obtained by setting a tilting angle as the initial guess for the FcC_6S anchored to the gold substrate with a Au–S distance of 2.39 Å [41] and then relaxed with DFT together to the first gold layer. The other gold atoms are fixed during the geometry relaxation. The geometry relaxation is performed in QuantumATK [42, 43] (v. S-2021.06-SP2) using DFT at the generalized gradient approximation (GGA) level within the framework of Perdew, Burke, and Ernzerhof (PBE) and double-ζ plus polarization (DZP) basis set for all elements except gold, for which single-ζ plus polarization (SZP) is used. Dirichlet boundary conditions (DBC) are applied in the transport direction, and periodic boundary conditions (PBC) in transverse directions. Limited memory quasi-Newton method for large scale optimization (LBFGS) optimization algorithm with force tolerance 0.05 eV/Å and maximum step size 0.02 Å is used.

Electronic structure properties of the $AuFcC_6S$ junction are studied in QuantumATK through the DFT with GGA, PBE, Hubbard (on-site-shell) correction for exchange-correlation terms, SZP for Au and DZP for other elements; k-points (3, 1, 135) with Monkhorst grid, sparse recursion method for self-energy calculation (both equilibrium and non-equilibrium). An additional continuum spatial region is placed within the simulation boundary cell, permitting to account for the electrostatic potential vanishment as it happens in a dielectric substrate, and avoiding abrupt potential decaying to zero, enforced at the boundary of the simulation cell.

The transport calculations are performed within the general NEGF formalism [44]. The transport equations are solved self-consistently with the system electrostatics, calculated by solving Poisson equation with the parallel conjugate gradient method with DBC in the transport direction and PBC in the transverse ones. The readout current I_R is computed through a Landauer-like formula for current [45]

$$I_R = \frac{2q}{h}\int_{-\infty}^{+\infty} T(E, V_B)\left(f_{NW}(E) - f_{E1}(E)\right) dE \quad (2)$$

where h is the Planck constant, E is the electron energy, V_B is the bias voltage, and f_{NW} and f_{E1} are the electrode Fermi-Dirac distributions. $T(E,V_B)$ is the transmission function representing the NW-to-E1 electron transmission probability of the device. Six bias points were considered from $V_B = 0$ to $V_B = 1$ V. In each of them, the $T(E)$ function and its integral (2) are calculated considering an energy array from −1 to 1 eV with 201 values; transverse k-point (Monkhorst grid) (7, 3); Krylov method for self-energy calculation.

Funding note: Open access funding provided by Politecnico di Torino within the CRUI-CARE Agreement.

Electronic Supplementary Material: Supplementary material (the molecule structure of the 6-(ferrocenyl)hexanethiol cation, the details regarding the method used to create electric fields in ORCA, and additional graphs) is available in the online version of this article at https://doi.org/10.1007/s12274-024-6811-2.

References

[1] Lent, C. S.; Tougaw, P. D.; Porod, W.; Bernstein, G. H. Quantum cellular automata. *Nanotechnology* **1993**, *4*, 49–57.

[2] Lent, C. S. Bypassing the transistor paradigm. *Science* **2000**, *288*, 1597–1599.

[3] Lent, C. S.; Isaksen, B.; Lieberman, M. Molecular quantum-dot cellular automata. *J. Am. Chem. Soc.* **2003**, *125*, 1056–1063.

[4] Lent, C. S.; Isaksen, B. Clocked molecular quantum-dot cellular automata. *IEEE Trans. Electron Devices* **2003**, *50*, 1890–1896.

[5] Arima, V.; Iurlo, M.; Zoli, L.; Kumar, S.; Piacenza, M.; Della Sala, F.; Matino, F.; Maruccio, G.; Rinaldi, R.; Paolucci, F. et al. Toward quantum-dot cellular automata units: Thiolated-carbazole linked bisferrocenes. *Nanoscale* **2012**, *4*, 813–823.

[6] Lu, Y. H.; Lent, C. S. A metric for characterizing the bistability of molecular quantum-dot cellular automata. *Nanotechnology* **2008**, *19*, 155703.

[7] Ardesi, Y.; Garlando, U.; Riente, F.; Beretta, G.; Piccinini, G.;

Graziano, M. Taming molecular field-coupling for nanocomputing design. *J. Emerg. Technol. Comput. Syst.* **2023**, *19*, 1.
[8] Blair, E. P.; Yost, E.; Lent, C. S. Power dissipation in clocking wires for clocked molecular quantum-dot cellular automata. *J. Comput. Electron.* **2010**, *9*, 49–55.
[9] Ardesi, Y.; Graziano, M.; Piccinini, G. A model for the evaluation of monostable molecule signal energy in molecular field-coupled nanocomputing. *J. Low Power Electron. Appl.* **2022**, *12*, 13.
[10] Blair, E. P.; Corcelli, S. A.; Lent, C. S. Electric-field-driven electron-transfer in mixed-valence molecules. *J. Chem. Phys.* **2016**, *145*, 014307.
[11] Wang, Y.; Lieberman, M. Thermodynamic behavior of molecular-scale quantum-dot cellular automata (QCA) wires and logic devices. *IEEE Trans. Nanotechnol.* **2004**, *3*, 368–376.
[12] Ardesi, Y.; Gaeta, A.; Beretta, G.; Piccinini, G.; Graziano, M. *Ab initio* molecular dynamics simulations of field-coupled nanocomputing molecules. *J. Integr. Circuits Syst.* **2021**, *16*, 1–8.
[13] Verstraete, L.; Szabelski, P.; Bragança, A. M.; Hirsch, B. E.; De Feyter, S. Adaptive self-assembly in 2D nanoconfined spaces: Dealing with geometric frustration. *Chem. Mater.* **2019**, *31*, 6779–6786.
[14] Christie, J. A.; Forrest, R. P.; Corcelli, S. A.; Wasio, N. A.; Quardokus, R. C.; Brown, R.; Kandel, S. A.; Lu, Y. H.; Lent, C. S.; Henderson, K. W. Synthesis of a neutral mixed-valence diferrocenyl carborane for molecular quantum-dot cellular automata applications. *Angew. Chem., Int. Ed.* **2015**, *54*, 15448–15451.
[15] Ardesi, Y.; Beretta, G.; Fabiano, C.; Graziano, M.; Piccinini, G. A reconfigurable field-coupled nanocomputing paradigm on uniform molecular monolayers. In *2021 International Conference on Rebooting Computing (ICRC)*, Los Alamitos, CA, USA, 2021, pp 124–128.
[16] Mallada, B.; Ondráček, M.; Lamanec, M.; Gallardo, A.; Jiménez-Martín, A.; de la Torre, B.; Hobza, P.; Jelínek, P. Visualization of π-hole in molecules by means of kelvin probe force microscopy. *Nat. Commun.* **2023**, *14*, 4954.
[17] Gross, L.; Mohn, F.; Liljeroth, P.; Repp, J.; Giessibl, F. J.; Meyer, G. Measuring the charge state of an adatom with noncontact atomic force microscopy. *Science* **2009**, *324*, 1428–1431.
[18] Liza, N.; Murphey, D.; Cong, P. Z.; Beggs, D. W.; Lu, Y.; Blair, E. P. Asymmetric, mixed-valence molecules for spectroscopic readout of quantum-dot cellular automata. *Nanotechnology* **2022**, *33*, 115201.
[19] Ardesi, Y.; Mo, F.; Spano, C. E.; Ardia, G.; Piccinini, G.; Graziano, M. Conformation-based molecular memories for nanoscale memcomputing. In *IEEE 23rd International Conference on Nanotechnology (NANO)*, Jeju Island, Korea, 2023, pp 694–697.
[20] Peng, J. B.; Sokolov, S.; Hernangómez-Pérez, D.; Evers, F.; Gross, L.; Lupton, J. M.; Repp, J. Atomically resolved single-molecule triplet quenching. *Science* **2021**, *373*, 452–456.
[21] Mishra, S.; Fatayer, S.; Fernández, S.; Kaiser, K.; Peña, D.; Gross, L. Nonbenzenoid high-spin polycyclic hydrocarbons generated by atom manipulation. *ACS Nano* **2022**, *16*, 3264–3271.
[22] Hieulle, J.; Castro, S.; Friedrich, N.; Vegliante, A.; Lara, F. R.; Sanz, S.; Rey, D.; Corso, M.; Frederiksen, T.; Pascual, J. I. et al. On-surface synthesis and collective spin excitations of a triangulene-based nanostar. *Angew. Chem., Int. Ed.* **2021**, *60*, 25224–25229.
[23] Mo, F.; Ardesi, Y.; Roch, M. R.; Graziano, M.; Piccinini, G. Investigation of amperometric sensing mechanism in gold-C_{60}-gold molecular dot. *IEEE Sensors J.* **2022**, *22*, 19152–19161.
[24] Mo, F.; Spano, C. E.; Ardesi, Y.; Roch, M. R.; Piccinini, G.; Graziano, M. Design of pyrrole-based gate-controlled molecular junctions optimized for single-molecule aflatoxin B1 detection. *Sensors* **2023**, *23*, 1687.
[25] Ardesi, Y.; Pulimeno, A.; Graziano, M.; Riente, F.; Piccinini, G. Effectiveness of molecules for quantum cellular automata as computing devices. *J. Low Power Electron. Appl.* **2018**, *8*, 24.
[26] Karadag, M.; Geyik, C.; Demirkol, D. O.; Ertas, F. N.; Timur, S. Modified gold surfaces by 6-(ferrocenyl)hexanethiol/dendrimer/gold nanoparticles as a platform for the mediated biosensing applications. *Mater. Sci. Eng.: C* **2013**, *33*, 634–640.
[27] Göver, T.; Yazıcıgil, Z. Electrochemical study of 6-(ferrocenyl)hexanethiol on gold electrode surface in non-aqueous media. *Surf. Interfaces* **2018**, *13*, 163–167.
[28] Csaba, G.; Imre, A.; Bernstein, G. H.; Porod, W.; Metlushko, V. Nanocomputing by field-coupled nanomagnets. *IEEE Trans. Nanotechnol.* **2002**, *1*, 209–213.
[29] Solomon, G. C.; Herrmann, C.; Hansen, T.; Mujica, V.; Ratner, M. A. Exploring local currents in molecular junctions. *Nat. Chem.* **2010**, *2*, 223–228.
[30] Ardesi, Y.; Turvani, G.; Graziano, M.; Piccinini, G. SCERPA simulation of clocked molecular field-coupling nanocomputing. *IEEE Trans. Very Large Scale Integr. VLSI Syst.* **2021**, *29*, 558–567.
[31] Beretta, G.; Ardesi, Y.; Piccinini, G.; Graziano, M. Vlsi-nanocomputing/scerpa: Scerpa v4.0.1. Zenodo, 2022.
[32] Neese, F. The ORCA program system. *Wiley Interdiscip. Rev.: Comput. Mol. Sci.* **2012**, *2*, 73–78.
[33] Neese, F. Software update: The ORCA program system, version 4.0. *Wiley Interdiscip. Rev.: Comput. Mol. Sci.* **2018**, *8*, e1327.
[34] Weigend, F.; Ahlrichs, R. Balanced basis sets of split valence, triple zeta valence and quadruple zeta valence quality for H to Rn: Design and assessment of accuracy. *Phys. Chem. Chem. Phys.* **2005**, *7*, 3297.
[35] Grimme, S.; Antony, J.; Ehrlich, S.; Krieg, H. A consistent and accurate *ab initio* parametrization of density functional dispersion correction (DFT-D) for the 94 elements H–Pu. *J. Chem. Phys.* **2010**, *132*, 154104.
[36] Grimme, S.; Ehrlich, S.; Goerigk, L. Effect of the damping function in dispersion corrected density functional theory. *J. Comput. Chem.* **2011**, *32*, 1456–1465.
[37] Breneman, C. M.; Wiberg, K. B. Determining atom-centered monopoles from molecular electrostatic potentials The need for high sampling density in formamide conformational analysis. *J. Comput. Chem.* **1990**, *11*, 361–373.
[38] Weigend, F. Accurate Coulomb-fitting basis sets for H to Rn. *Phys. Chem. Chem. Phys.* **2006**, *8*, 1057–1065.
[39] Thompson, A. P.; Aktulga, H. M.; Berger, R.; Bolintineanu, D. S.; Brown, W. M.; Crozier, P. S.; in 't Veld, P. J.; Kohlmeyer, A.; Moore, S. G.; Nguyen, T. D. et al. LAMMPS—A flexible simulation tool for particle-based materials modeling at the atomic, meso, and continuum scales. *Comput. Phys. Commun.* **2022**, *271*, 108171.
[40] Aktulga, H. M.; Fogarty, J. C.; Pandit, S. A.; Grama, A. Y. Parallel reactive molecular dynamics: Numerical methods and algorithmic techniques. *Parallel Comput.* **2012**, *38*, 245–259.
[41] Rodriguez, J. A.; Dvorak, J.; Jirsak, T.; Liu, G.; Hrbek, J.; Aray, Y.; González, C. Coverage effects and the nature of the metal–sulfur bond in S/Au(111): High-resolution photoemission and density-functional studies. *J. Am. Chem. Soc.* **2003**, *125*, 276–285.
[42] Smidstrup, S.; Markussen, T.; Vancraeyveld, P.; Wellendorff, J.; Schneider, J.; Gunst, T.; Verstichel, B.; Stradi, D.; Khomyakov, P. A.; Vej-Hansen, U. G. et al. Quantumatk: An integrated platform of electronic and atomic-scale modelling tools. *J. Phys.: Condens. Matter* **2020**, *32*, 015901.
[43] Smidstrup, S.; Stradi, D.; Wellendorff, J.; Khomyakov, P. A.; Vej-Hansen, U. G.; Lee, M. E.; Ghosh, T.; Jónsson, E.; Jónsson, H.; Stokbro, K. First-principles Green's-function method for surface calculations: A pseudopotential localized basis set approach. *Phys. Rev. B* **2017**, *96*, 195309.
[44] Brandbyge, M.; Mozos, J. L.; Ordejón, P.; Taylor, J.; Stokbro, K. Density-functional method for nonequilibrium electron transport. *Phys. Rev. B* **2002**, *65*, 165401.
[45] Datta, S. *Quantum Transport: Atom to Transistor*; Cambridge University Press: Cambridge, 2005.